ADVANCED FUNCTIONAL MATERIALS
www.afm-journal.de

Surface Reduced Manganese States as a Source of Oxygen Reduction Activity in $BaMnO_3$

Lucia Hughes, Ahin Roy,* Clive Downing, Michelle P. Browne, Ainur Zhussupbekova, Igor V. Shvets, and Valeria Nicolosi**

In relation to perovskites, tweaking the oxidation state of the B-site cation is fundamental to controlling the catalytic activity of these materials, thus necessitating a complete characterization of surface oxidation states. Herein, using a combination of atomic-scale imaging and spectroscopic techniques, structure-property correlation in barium manganese oxide ($BaMnO_3$) is established for the oxygen reduction reaction (ORR). Electron energy loss spectroscopy (EELS) on the synthesized $BaMnO_3$ find the rods to contain an amorphous surface layer with reduced Mn^{3+} states compared to Mn^{4+} states in the bulk. Consequently, the $BaMnO_3$ rods show electrocatalytic activity for the ORR, which originates from the presence of Mn^{3+} at the rod surface. Furthermore, heating of the samples in air at 300 and 800 °C results in a decrease in the number of Mn^{3+} states, and thus lowering of the ORR activity. This study represents a step-stone study in understanding the mechanism of ORR activity and its association to the Mn^{3+} state at the perovskite's surface, opening up possibilities for further surface engineering and tuning catalytic properties.

1. Introduction

Today's society and researchers are challenged with developing electrochemical technologies for energy storage and conversion that can perform safely, and are competitive with the performance and cost of fossil fuels. The oxygen reduction reaction (ORR) is at the heart of energy conversion and storage technologies, including energy storage devices, e.g., metal–air batteries and energy conversion devices, e.g., fuel cells. Thus, it has become one of the main focuses in the field of electrocatalysis.[1–3] While marketed usage of metal–air batteries still needs development, fuel cells are already in deployment in various energy sectors. In fuel cells, the ORR is the immediate reaction taking place at the cathode, but the problematic activation and cleavage of the O_2 double bond means that it is kinetically slow, and is considered a key bottleneck in their performance.[4–6] Therefore, for practical device performance and widespread use of fuel cell technologies, such as solid-oxide fuel cells, proton-exchange membrane fuel cells, and direct methanol fuel cells, a catalyst is required to speed up the kinetics of this reaction. Platinum-based catalysts form the benchmark for ORR electrocatalysis.[7,8] However, their use is not suitable for large-scale applications due their limited reserves and high-cost. As a result, significant efforts have been devoted to designing and developing suitable low-cost, high-performing electrocatalytic materials to replace the use of platinum and other precious metal-based catalysts.[9–12]

In recent decades, perovskites have emerged as an alternative to the precious metal catalysts used for ORR, owing to their low-cost, high chemical stability, diversity, and tunability of their surface oxidation states.[13–20] With a general structure of ABO_3, variation of the A- or B-site cation, and/or the creation of

L. Hughes, A. Roy, A. Zhussupbekova, V. Nicolosi, I. V. Shvets
Advanced Microscopy Laboratory
Trinity College Dublin
Dublin 2, Ireland
E-mail: hugheslu@tcd.ie; ahinroy@matsc.iitkgp.ac.in; nicolov@tcd.ie

L. Hughes, A. Roy, C. Downing, M. P. Browne, V. Nicolosi
School of Chemistry
Trinity College Dublin
Dublin 2, Ireland

The ORCID identification number(s) for the author(s) of this article can be found under https://doi.org/10.1002/adfm.202214883.

L. Hughes, A. Roy, M. P. Browne, V. Nicolosi
Centre for Research of Adaptive Nanostructures and Nanodevices (CRANN) & Advanced Materials and Bioengineering Research Centre (AMBER)
Trinity College Dublin
Dublin 2, Ireland

A. Roy
Materials Science Centre
Indian Institute of Technology Kharagpur
Kharagpur, West Bengal 721302, India

M. P. Browne
Helmholtz-Zentrum Berlin für Materialien und Energie
14109, Berlin, Germany

A. Zhussupbekova, I. V. Shvets
School of Physics
Trinity College Dublin
Dublin 2, Ireland

DOI: 10.1002/adfm.202214883

oxygen vacancies influences the perovskite chemical and structural composition, and thus catalyst performance.[21–24] As a result, significant efforts have been devoted to the identification of suitable activity descriptors with links established between the electrocatalytic activity of ABO_3 perovskites and the nature, coordination and thus orbital occupancy of the B-site transition metal cation.[11,25,26] However, such efforts have mainly focused on bulk structure-activity descriptors with the thorough atomic-scale assessment and analysis of perovskite surfaces remaining elusive.[27,28] Atomic-scale imaging and spectroscopy using electron microscopy offers the opportunity to bridge the gap, enabling the correlation between the surface atomic-structure and chemical nature with the electrocatalytic activity.[29]

Given the influence of surface composition on the corresponding activity of materials, the elemental segregation and/or phase separation, which is a common phenomenon at perovskite surfaces, is an important factor to consider. In fact, the dominant presence of inactive A-site cations at the surface creates a key issue in the utilization of perovskites in electrocatalysis, and highlights the importance of targeting the less accessible B-site terminated structure.[30] Barzilay et al. displayed the ability to pattern TiO_x sites at the surface of $BaTiO_3$ nanoparticles by using electron beam irradiation.[31] Meanwhile, Wang et al. have engineered the Mn-termination of $La_{0.45}Sr_{0.45}MnO_3$ via a simple one-pot hydrothermal method.[32] When compared with other transition metal cations, Mn-containing perovskite materials display greater ORR activity reflecting the electrocatalytic performance of even simple Mn-containing oxides, such as α-MnO_2.[33,34] Unlike precious metal-based catalysts, oxide catalysts mediate electrochemical processes through surface redox reactions.[11] Furthermore, Celorrio et al. have shown that the onset potential for ORR overlaps with the reduction potential of Mn cations, and have proposed that this is the key rationale behind the high activity of Mn-containing oxides.[35]

This work assesses the dependence of the electrocatalytic activity of $BaMnO_3$ rods on their atomic surface structure and composition by utilizing various electron microscopic techniques, in combination with spectroscopic methods. $BaMnO_3$ rods with a high degree of phase purity are synthesized by a low temperature low pressure hydroxide-mediated method. Atomic-resolution scanning transmission electron microscopy (STEM) imaging and electron energy loss spectroscopy (EELS) are used to investigate the surface structure and composition, respectively. EELS was partnered with X-ray photoelectron spectroscopy (XPS) to determine the chemical states present at the surface of as-synthesized and annealed samples, and the effects such states have on the corresponding ORR activity. The findings in this study provide atomic-scale evidence for the dependence of ORR activity on the presence of Mn^{3+} states in $BaMnO_3$ rods. As a result, this work displays the importance of atomic-scale structural and chemical analyses in understanding the ORR activity of perovskite materials and provides insights into avenues for future surface engineering and optimization of catalytic performance.

2. Results and Discussion

The hydroxide composite-mediated method used in this work provides a simple, versatile and cost-effective approach for synthesizing crystalline and chemically pure $BaMnO_3$ rods at low temperatures and pressures.[36] This is in stark contrast to the harsh temperatures and pressures involved in the sequential firing and grinding steps traditionally used for the synthesis of perovskite materials, making this synthesis approach widely applicable and more environmentally-friendly. The possible reaction mechanism of this synthesis method can be described as follows:[37]

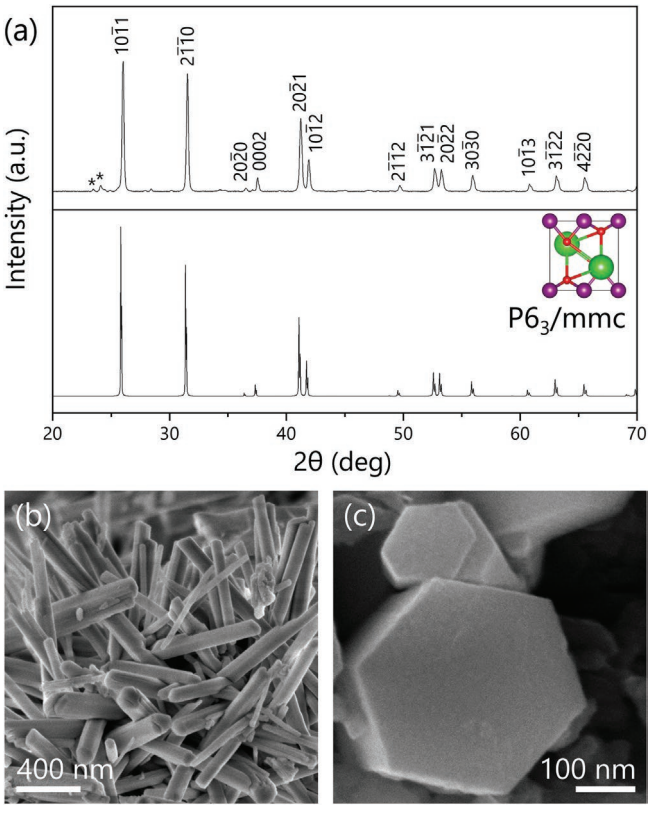

Figure 1. Perovskite $BaMnO_3$ rods synthesized via a hydroxide composite-mediated approach. a) Experimental XRD pattern (upper panel) compared with a 2H-$BaMnO_3$ reference pattern (lower panel). The unit cell of the 2H-$BaMnO_3$ crystal structure is shown in the inset with Ba atoms in green, Mn atoms in purple and O atoms in red. b,c), respectively, are SEM images of the $BaMnO_3$ rods displaying their hexagonal morphology and well-faceted surfaces.

$$BaCl_2 + 2NaOH \rightarrow Ba(OH)_2 + 2NaCl \quad (1)$$

$$MnO_2 + 2NaOH \rightarrow Na_2MnO_3 + H_2O \quad (2)$$

$$Ba(OH)_2 + Na_2MnO_3 \rightarrow BaMnO_3 + 2NaOH \quad (3)$$

where NaOH can be replaced with KOH. The morphology and crystal structure of the as-synthesized rods are displayed in **Figure 1**. The X-ray diffraction (XRD) pattern in Figure 1a reveals a high degree of phase purity with the exception of two small peaks ≈24° (marked with *), corresponding to a trace amount of residual raw materials.[38,39] All peaks are well indexed with the hexagonal 2H-$BaMnO_3$ crystal structure (JCPDS no. 26-0168) with space group $P6_3/mmc$ and lattice parameters $a = b = 5.6991$ and $c = 4.8148$ Å. In contrast to other

hexagonal perovskite phases which contain repeated series of face-sharing and corner-sharing MnO_6 octahedra, here the 2H indicates the presence of a continuous chains of face-sharing MnO_6 octahedra along the *c*-axis. This phase corresponds with that predicted by the Goldschmidt tolerance factor ($t = (r_A + r_O)/\sqrt{2}\ (r_B + r_O) = 1.06$), as a deviation in this value above unity corresponds with face-sharing MnO_6 octahedra links which are required in order to expand the A-sites for the large Ba^{2+} ions.[40] Representative scanning electron microscopy (SEM) images of the $BaMnO_3$ rods in Figure 1b,c clearly show the hexagonal shape and well-defined facets of the rods. The rods have widths which range from tens of nm to 400 nm, whereas their lengths vary from <1 to 6 µm. This was confirmed via low magnification STEM imaging and subsequent size distributions, which are displayed in Figure S1 (Supporting Information). Despite the large variation in size of the rods, the hexagonal morphology remains consistent throughout all rods.

Transmission electron microscopy (TEM) imaging and selected area electron diffraction (SAED) were performed to further confirm the crystallinity and structure of the $BaMnO_3$ rods. The low magnification TEM image in **Figure 2**a confirms the rod-like structure of the as-synthesized powder. The SAED pattern and high-resolution transmission electron microscopy (HRTEM) image in Figure 2b,c reveal the crystallinity and growth modality of the rods. Complementary to the XRD pattern in Figure 1a, the SAED spots and the spacings of the lattice fringes in the HRTEM image can be indexed to the 2H-$BaMnO_3$ structure. The spot pattern of the SAED indicates that the rods are single crystalline. The lattice fringes in the HRTEM image can be indexed to the $(10\bar{1}0)$ and (0001) planes with interplanar distances 0.49 and 0.48 nm, respectively. By combining the indexing of the diffraction pattern with the planes identified in the HRTEM image, a growth direction of [0001] can be determined, which is expected, as there is an inherent crystallographic anisotropy along the *c*-direction in hexagonal structures.[36,37,39]

Atomic-resolution high-angle annular dark-field (HAADF) STEM imaging was used to confirm the atomic structure of the rods. HAADF STEM imaging, also termed as *Z*-contrast imaging, leads to image contrast which is highly dependent on the atomic number ($Z^{\sim 2}$) of the scattering element.[41,42] Therefore, by examining the HAADF STEM image in Figure 2d the positions of the Ba and Mn atoms within the planes can be deduced, with the Ba atoms appearing brighter due to their heavier atomic weight. The O atoms are too light to be detected in such images, due to the insensitivity of HAADF STEM imaging to light elements.[43] The continuous series of Mn atoms in the horizontal plane of the image in Figure 2d confirms the formation of the 2H-$BaMnO_3$ crystal structure. By comparing the atomic structure with the theoretical structure displayed in Figure 2f, as well as the simulated HAADF STEM image in Figure 2e, one can confidently conclude that the rods exhibit the 2H-perovskite structure.

STEM imaging at the surface of the $BaMnO_3$ rods reveals an amorphous surface layer as shown in **Figure 3**a. The presence of such a layer was found to be consistent for all rods and ranged in thickness from 1 to 2 nm.

In support of the structural analysis of the surface, EELS was carried out on the surface region to probe its chemical nature. EELS is a powerful spectroscopic technique by which the local electronic state and coordination environment of the Mn atoms can be investigated by observing the Mn $L_{2,3}$-edge.[44–46]

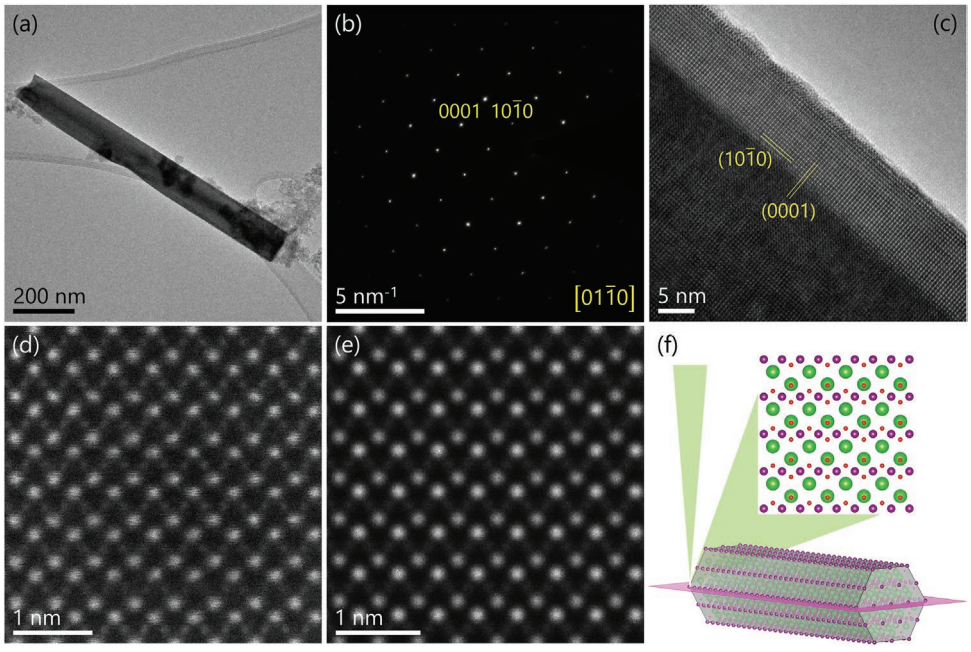

Figure 2. Perovskite $BaMnO_3$ morphology, crystallography and atomic structure. a) Low magnification TEM image of a single $BaMnO_3$ rod. b) SAED pattern and c) corresponding HRTEM image of an average $BaMnO_3$ rod with markings of the plane reflections and lattice fringes, respectively, from the $(10\bar{1}0)$ and (0001) planes. Both the SAED pattern and HRTEM image were captured from the $[01\bar{1}0]$ zone axis. d) Experimental and e) simulated HAADF STEM images of the $BaMnO_3$ rods from the $[10\bar{1}0]$ zone axis. f) A schematic illustration of the imaging process of the $(10\bar{1}0)$ 2H-$BaMnO_3$ crystal structure.

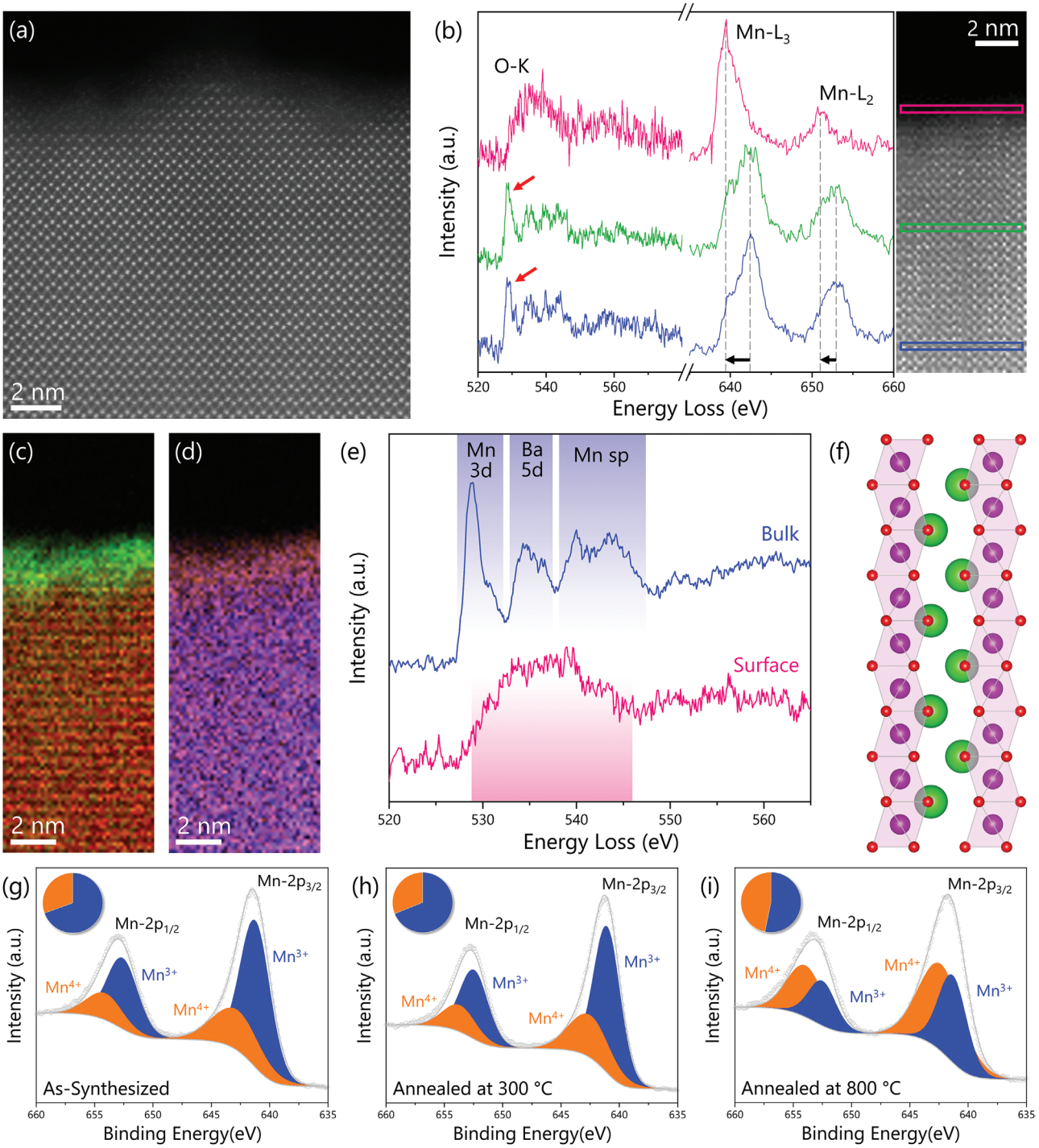

Figure 3. Surface analysis of perovskite $BaMnO_3$ rods. a) HAADF STEM image of $BaMnO_3$ displaying the bulk crystal structure, and showing the presence of an amorphous layer at the surface of the rods. b) Spatially resolved O *K*-edge and Mn *L*-edge EELS spectra from the bulk and surface of the rods. The red arrows indicate the presence of a pre-edge feature in the O *K*-edge EELS spectra from the bulk of the rod. The black arrows are used to indicate the shift in the Mn L_3 and L_2 peaks when traversing from the bulk to the surface. c) Chemical map showing the localization of reduced Mn states within the surface layer (green) and Mn^{4+} states within the bulk of the rods (red). d) Chemical map of the O *K*-edge (orange) and the prevalence of the pre-peak signal (blue) within the bulk of the rods. e) O-*K* edge EELS spectra averaged over an area of 5.9 × 1.2 nm in the bulk and surface layer of the rods, with an overlay of the ELNES details. f) A schematic illustration of the 2H-$BaMnO_3$ bulk crystal structure displaying the octahedral coordination of Mn. High resolution Mn 2*p* XPS spectra of the g) as-synthesized rods, and those annealed at h) 300 and i) 800 °C in air. A representative display of the Mn^{4+}:Mn^{3+} ratios are shown within the insets.

Figure 3b displays the Mn $L_{2,3}$-edge consisting of two peaks, L_3 and L_2, which correspond to the energy loss caused by promoting electron transitions from the $2p_{3/2}$ and $2p_{1/2}$ states, respectively, to unoccupied 3*d*-bands. Additionally, the energy

separation between the L_3 and L_2 peaks reflects the spin orbit splitting of the initial states in the transition, and varies with atomic number.[47] Meanwhile, the L_3/L_2 intensity ratio, also known as the white-line intensity ratio, is dependent on the spin-spin coupling and interactions between the initial and final states.[48,49] As a result, it can be related to the oxidation state of the metal with the aid of detailed chemical information.[47] By relating the spatially resolved Mn $L_{3,2}$-edge EELS spectra in Figure 3b to the HAADF STEM image of the mapped area displayed within the same figure, it is clear that there is a chemical shift in the Mn L_3 and L_2 peaks between the bulk of the rods and the amorphous layer at the surface. However, despite the observation of this shift, the absolute values of the energy thresholds are difficult to obtain experimentally, and for this reason all energy scales with respect to the EELS spectra are assumed to be approximate.[50] With that being said, the shift in the Mn $L_{2,3}$-edge can be related to the variation in the Mn oxidation state, and thus the oxygen vacancy content when traversing from the bulk to the surface of the $BaMnO_3$ rods. The Mn L_3 peak at the surface is ≈3.0 eV lower in energy than that in the bulk, whereas the Mn L_3/L_2 intensity ratio and energy separation are smaller in the bulk than at the surface. Due to an increase in the effective charge on the metal site with increasing oxidation state, the Mn $L_{3,2}$-edge shows higher energy loss for Mn ions with higher oxidation state.[45,51] Similarly, the Mn L_3/L_2 intensity ratio decreases with increasing oxidation state due to a decrease in the $2p$–$3d$ exchange interaction.[52] Therefore, such changes in peak position and peak ratio correspond to a higher Mn oxidation state within the bulk of the rods compared to the surface layer. Due to the natural valence state of Ba and O, it can be assumed that Mn exists as the Mn^{4+} state within the bulk of the rods, and thus the states at the surface can be characterized as $Mn^{(4-x)+}$ states. It is important to note that although the L_3/L_2 intensity ratio is undoubtedly the most popular and common method used to relate EELS spectra to the oxidation state of transition metal ions, its value is highly dependent on the sample thickness, and is sensitive to the size and position of the integration window, as well as the various empirical algorithms and parameters used in its calculation.[53] This is particularly important to consider in this case as the thickness of the rods, and thus the presence of plural scattering, varies greatly across the width of the rods as shown in Figure S4 (Supporting Information). Therefore, the shift in the $L_{3,2}$-edge position and variation in the L_3/L_2 intensity ratio are both used here to deduce a decrease in the oxidation state of Mn within the amorphous surface layer of the rods, while other spectroscopic techniques are employed to quantitatively analyze the presence of different Mn oxidation states.

Due to the high dependence of EELS on coordination environment and the octahedral bonding between the Mn and O atoms in $BaMnO_3$, the O *K*-edge plays an important role in the investigation of Mn oxidation state and oxygen vacancy concentration. In fact, by nature the *K*-edge is much more closely related to the atomic coordination than the *L*-edge.[53] By correlating the spatially resolved O *K*-edge EELS spectra in Figure 3b to the HAADF STEM image of the mapped area, the existence of a pre-peak in the O *K*-edge becomes evident within the bulk of the rods, but disappears when traversing to the amorphous layer at the surface. Taking a closer look at the O *K*-edge EELS spectrum averaged over a larger area, the energy loss near-edge structure (ELNES) can be determined as shown in Figure 3e. The ELNES reveals that the O *K*-edge can be divided into three distinct regions as a result of the hybridization of the O $2p$ orbitals with the Mn $3d$, Ba $5d$, and Mn $4sp$ orbitals.[54,55] The perovskite structure consists of MnO_6 octahedra for which crystal field splitting results in $2t_{2g}$ states that are essentially purely π bonded and $3e_g$ states that are purely σ bonded. This is often reflected in the pre-peak which is subsequently split into two peaks; the stronger σ interactions increases the dispersion of the e_g band such that the t_{2g} band appears more intense and narrower.[56] In Figure 3e, the pre-peak consists of an intense peak with a shoulder on the higher energy side. In this instance, the e_g band is less prominent due to multiple scattering effects, and thus is demoted to a shoulder peak.[57] The third region of the spectrum extends far beyond the onset of the edge due to the hybridization of O $2p$ states with weakly structured metallic $4sp$ states.[57] Thus, it is clear that the intensity of the O *K*-edge pre-peak is indicative of the number of unoccupied Mn $3d$ states projected at the O atom. Therefore, the onset energy can be correlated with the Mn oxidation state, such that it increases in energy position with decreasing transition metal oxidation state.[58–60] However, in this instance the pre-peak very clearly disappears in traversing from the bulk to the surface of the rods, as do the distinctive regions of the ELNES. The difference in the O *K*-edge features between the bulk and surface layer can be attributed to the rearrangement of the bulk crystal structure at the surface, the formation of oxygen vacancies and/or the destruction of long range order.[61,62] Such structural distortions (i.e., changes to the octahedral coordination) would lead to fewer and less efficient hybridization between O $2p$ and Mn states, thus resulting in a reduction in the O *K*-edge ELNES. Complimentary to the changes in the Mn $L_{3,2}$-edge when traversing from the bulk to the surface of the rods, the disappearance of the pre-peak in the O *K*-edge can also be related to the reduction of neighboring Mn atoms.[63]

Along with the STEM-EELS analysis, XPS was carried out on the as-synthesized powder to probe the surface further and identify the Mn oxidation states. Figure 3g shows the high-resolution XPS spectrum acquired in the Mn $2p$ region (the full XPS survey and corresponding high-resolution spectra from the Ba and O regions can be found in Figure S5, Supporting Information). Regarding the interpretation of Mn oxidation states, spin orbit coupling doublet peaks were detected attributing to the Mn $2p_{3/2}$ and $2p_{1/2}$ states. The fitted peaks positioned at 642.8 and 654.0 eV correspond to the Mn^{4+} state, whereas those positioned at 641.2 and 652.6 eV correspond to the Mn^{3+} state, in agreement with previous reports.[64,65] The spectrum was not fitted with peaks corresponding to the Mn^{2+} state because the satellite peak associated with the Mn^{2+} state was not present.[66] Despite the small energy differences between the binding energy values of different Mn oxidation states and the associated complications with deconvoluting the Mn $2p$ doublet peaks, we were able to identify the presence of both Mn^{4+} and Mn^{3+} states.[67] This confirms the identification of Mn^{3+} states as the reduced Mn states within the amorphous surface layer of the $BaMnO_3$ rods.

To investigate the effects of post-modification annealing on the presence of different Mn oxidation states, as-synthesized $BaMnO_3$ rods were annealed at 300 and 800 °C for 24 h in air. Figure 3h shows the high-resolution XPS spectrum acquired from the Mn 2*p* region for the $BaMnO_3$ rods annealed in air at 300 °C for 24 h (the full XPS surveys and corresponding high-resolution spectra from the Ba and O regions for samples annealed at 300 and 800 °C can be found in Figure S5, Supporting Information). Again, the presence of both Mn^{4+} and Mn^{3+} states was detected with fitted peaks positioned at 642.5 and 653.7 eV, and 641.0 and 652.5 eV, respectively. A similar process was carried out for those annealed at 800 °C as shown in Figure 3i with peaks fitted at 642.3 and 653.9 eV, and 641.3 and 652.5 eV for the Mn^{4+} and Mn^{3+} states, respectively. By analyzing the peak areas, the reduction in the number of Mn^{3+} states with heating becomes evident. The percentage of Mn^{3+} states decreases from 69.5% to 68.9% for samples annealed at 300 °C. This drops significantly to 39.5% for those annealed at 800 °C. Consequently, the percentage of Mn^{4+} states increases from 30.5 to 31.1 and 60.5% when heated at 300 and 800 °C, respectively. The decrease in the percentage of Mn^{3+} states is evidence for the oxidation of the surface during annealing. Such changes to the chemical nature of the rod surface are accompanied by changes to the morphology of the rods, resulting in the rounding of the rod ends as seen in Figure S6 (Supporting Information). Despite such alterations to the rod surface and morphology, the atomic structure remains unchanged with heating as shown by the XRD and SAED patterns in Figure S6 (Supporting Information). It is important to note here that the STEM-EELS analysis of the annealed rods confirmed the perseverance of the amorphous layer and Mn^{3+} state at the surface of the rods after heating, as displayed in Figure S7 (Supporting Information). Although this seems to be countering the XPS data, it is important to note that STEM is a 2D projection of the 3D rods, and annealing induced oxidation may not be uniform across the rod surface.

With the confirmation of reduced Mn states present within the surface layer, and given the surface specificity of electrocatalytic processes, the as-synthesized $BaMnO_3$ rods, as well as those heated at 300 and 800 °C were tested for their electrocatalytic activity. In fact, the electrochemical responses of Mn-containing perovskite materials are very sensitive to the coordination, and hence oxidation state of the surface Mn sites.[25] The ORR activity was evaluated by linear sweep voltammetry (LSV) measurements as shown in **Figure 4**a. Corresponding LSVs recorded in a nitrogen degassed electrolyte are included in Figure S8 (Supporting Information) to confirm that the measured activity is due to the reduction of oxygen and not any other reaction. Based on the significantly more positive half-wave potential of the as-synthesized $BaMnO_3$ rods in comparison to the glassy carbon electrode, the activity of $BaMnO_3$ was confirmed. Furthermore, it is clear that the activity of the as-synthesized $BaMnO_3$ is superior to the rods annealed at 300 and 800 °C, with half-wave potentials of 0.663, 0.659, and 0.638 V versus RHE (reversible hydrogen electrode, against which all potentials in this manuscript are reported), respectively. In fact, samples annealed at 800 °C show very little activity above the level of the glassy carbon electrode. Additionally, the samples can be compared using their potential at a standard current density of –0.1 mA cm^{-2}, for which an inverse linear dependence on annealing temperature was detected as shown in Figure 4b. Again, the as-synthesized $BaMnO_3$ proves to be superior with a potential of 0.729 V compared to 0.699 and 0.638 V for samples annealed at 300 and 800 °C. Further electrochemical characterization of as-synthesized and annealed $BaMnO_3$, including stability tests, mass activity, impedance studies, and electron transfer number, can be found in the Supporting Information.

The superiority of as-synthesized samples can be related to the Mn states present at the surface of the rods. As-synthesized and annealed samples both contain Mn^{4+} states within the bulk crystal structure and Mn^{3+} states within the amorphous surface layer. However, as unveiled via XPS, the as-synthesized

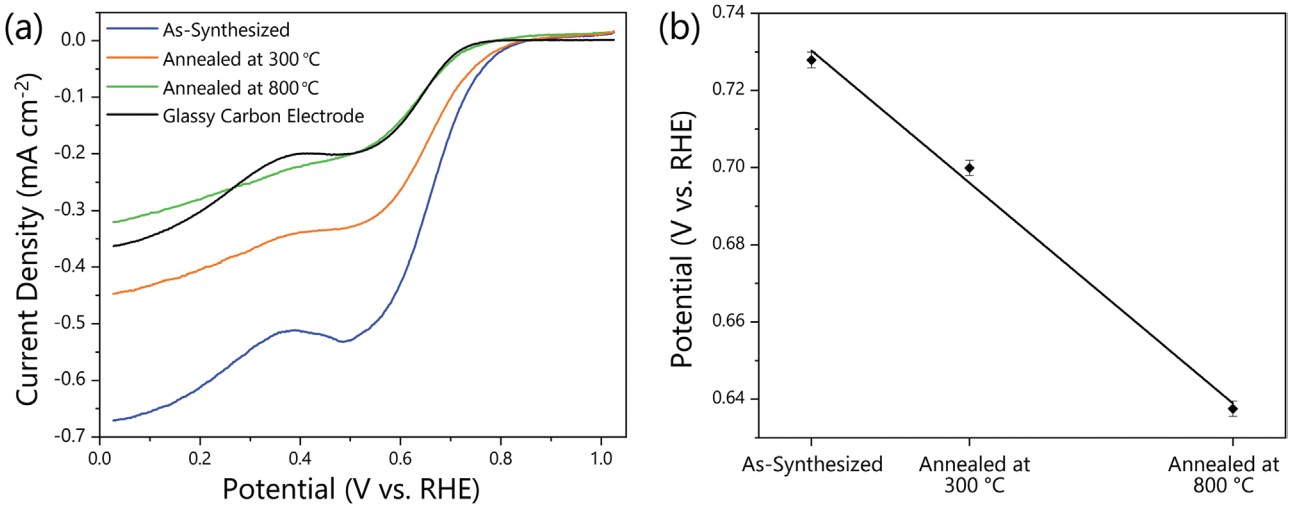

Figure 4. Structure-property correlation of the $BaMnO_3$ rods with respect to the ORR electrocatalytic activity. a) LSV measurements of as-synthesized and annealed $BaMnO_3$ and glassy carbon electrode. b) The dependence of the ORR potential recorded at a current density of –0.1 mA cm^{-2} on the annealing temperature ($R^2 = 0.989$).

$BaMnO_3$ rods contain a greater number of Mn^{3+} states when compared with the annealed samples. Therefore, due to the nature of electrocatalysis and the isolation of activity to the surface layer, it can be concluded that in this case the Mn^{3+} state has a higher activity for the ORR than the Mn^{4+} state. This is in agreement with previous reports on the electrocatalytic activity of Mn-containing perovskite materials.[21,68–70] The ORR process has no degradative effects on the $BaMnO_3$ structural or chemical nature with the amorphous layer and presence of the Mn reduced states remaining after testing, as shown in Figure S13 (Supporting Information). Furthermore, the ORR activity of perovskite materials is governed by the e_g occupancy of the transition metal ion, resulting in a volcano trend that states an e_g orbital electron occupancy close to unity will give the best ORR activity.[11,24] This is consistent with the logic that the e_g orbitals of the transition metal ion, rather than the t_{2g} orbitals, interact more easily with the O 2*p* orbitals to produce an adsorbed intermediate in the ORR reaction with an end-on adsorption mode, thus allowing for a covalent interaction with the adsorbate.[71] Assuming a high-spin configuration the Mn^{3+} state gives a $t_{2g}^3 e_g^1$ electronic configuration, whereas the Mn^{4+} state gives a $t_{2g}^3 e_g^0$ electronic configuration. Therefore, the Mn^{3+} state can be characterized as having an e_g occupancy equal to 1, thus its presence explains the superior electrocatalytic activity of the as-synthesized $BaMnO_3$. Conversely, the oxidation that occurs during the annealing process results in the reduction in the number of Mn^{3+} states, thus decreasing the effective e_g occupancy and lowering the ORR activity.

3. Conclusion

Single crystalline rods of $BaMnO_3$ were synthesized via a simple and cost-effective method, which is in stark contrast to the harsh temperatures and pressures traditionally used for perovskite syntheses. As-synthesized rods displayed the hexagonal 2H-perovskite structure with continuous chains of face-sharing MnO_6 octahedra along the *c*-axis. STEM and EELS analyses revealed the presence of an amorphous layer at the surface of the rods, containing reduced Mn states. XPS identified the surface states as Mn^{3+} states and confirmed that those within the bulk are in fact Mn^{4+} states. The as-synthesized $BaMnO_3$ rods displayed electrocatalytic activity for the ORR, however, such activity was found to decrease with annealing temperature. Therefore, the ORR activity was attributed to the presence of Mn^{3+} states at the surface and an electronic configuration that results in an e_g orbital occupancy value equal to 1.

4. Experimental Section

$BaMnO_3$ Rod Synthesis: The $BaMnO_3$ rods were synthesized based on a low-temperature, low-pressure, hydroxide composite-mediated method previously reported in literature.[37] The method was based on a reaction between the precursor metallic oxide and metallic salt in a molten hydroxide solution. A mixture of NaOH and KOH (20 g, NaOH:KOH = 51.5:48.5) was placed in a Teflon vessel. Stoichiometric amounts of MnO_2 and anhydrous $BaCl_2$ were added to the vessel, which was covered and shaken to ensure uniformly mixed reactants. The reaction was carried out in a furnace at 200 °C for 24 h. Once completed, the vessel and its contents were allowed to cool to room temperature within the furnace. Hot deionized water was used to dissolve the solid hydroxide mixture and release the solid product, which was subsequently washed with hot and room temperature deionized water until neutral pH. The product was dried in air at 75 °C for 6 h. Annealed samples were prepared by heating the as-synthesized powder in air at 300 and 800 °C for 24 h.

Characterization: Crystalline phase identification was carried out by powder XRD using a Bruker D8 Discover diffractometer with a Cu Kα radiation source, Goeble mirror, and Ge double bounce monochromator. For electron microscopy, the samples were added to deionized water and ultrasonically dispersed. A drop of the resulting dispersion was deposited on a lacey-carbon coated Cu grid and dried in vacuum overnight. The morphology and size of the as-synthesized powder were determined via SEM using a Zeiss Ultra Plus. Further analysis was carried out using TEM imaging, SAED, HRTEM, and low magnification STEM imaging on an uncorrected FEI Titan S-FEG dual TEM/STEM operated at 300 kV. Atomic-scale STEM imaging and EELS experiments were performed on a Nion UltraSTEM operated at 200 kV and equipped with a Gatan Enfinium EELS spectrometer. The spectra were acquired and processed using Gatan Digital Micrograph using a dispersion of 0.1 eV ch^{-1}, a collection angle β = 40 mrad and an exposure time of 20 ms px^{-1}. Energy filtered images, and subsequent t/λ maps, were acquired at 300 kV on an FEI Titan TEM/STEM with a Gatan Tridium Energy Filtering system. As-synthesized and annealed samples were prepared for XPS measurements by attaching the powders to carbon tape, mounting them on a stainless steel sample holder, and degassing them for ≈2 days in 10^{-9} to 10^{-10} mbar. XPS spectra were recorded using an Omicron Multi-Probe XPS instrument, with high-resolution spectra obtained at a 50 eV pass energy with a monochromatic Al Kα radiation source. The obtained spectra were analyzed in the CasaXPS software, in which an iterated Shirley background procedure was carried out and the high-resolution XPS peaks were fitted using Gaussian–Lorentzian shape fitting. All energetic positions were corrected with respect to the C 1s peak at 284.8 eV. By calculating the peak areas, the percentage of the relevant chemical states were determined.

Electrochemical Measurements: Electrochemical measurements for the as-synthesized and annealed samples were conducted in a typical three-electrode system on a Gamry workstation at room temperature. A carbon rod and Hg/HgO electrode were used as the counter and reference electrodes, respectively, with NaOH (1 M) as the electrolyte. To prepare the working electrode the $BaMnO_3$ powder (10 mg) was ultrasonically dispersed in a solution containing deionized water (500 µL), ethanol (400 µL), and Nafion 117 solution (4 µL). The resulting dispersion (5 µL) was dropcasted on a pre-polished glassy carbon rotating disk electrode (3 mm), and dried at 40 °C. Once dry, the electrode was connected to a rotating-disc set-up. For each of the active materials, an LSV was recorded without degassing the electrolyte, followed by an LSV recorded in an electrolyte degassed with N_2 for 15 min. All LSVs were recorded at a scan rate of 10 mV s^{-1}, a rotation rate of 1600 rpm and all potentials were reported against RHE using V versus RHE = V versus Hg/HgO + 0.926 V.

Supporting Information

Supporting Information is available from the Wiley Online Library or from the author.

Acknowledgements

L.H. and A.R. contributed equally to this work. The authors acknowledge the Advanced Microscopy Laboratory for the provision of their facilities. Microscopy characterization and analysis has been performed at the CRANN Advanced Microscopy Laboratory (AML) (www.tcd.ie/crann/aml/). The authors would also like to acknowledge Seán Ryan for his input on the impedance studies. The authors wish to thank

the support of the ERC CoG, 3D2DPrint (GA 681544) and SFI AMBER (12/RC/2278_P2), and Frontiers for the Future (20/FFP-A/8950). L.H. would like to acknowledge the support of the IRC through award no. GOIPG/2019/2642. M.P.B. would like to acknowledge the European Union's Horizon 2020 Research and Innovation Programme under the Marie Skłodowska-Curie grant agreement no. 884318 (TriCat4Energy). In addition, A.Z. would also like to acknowledge the funding from IRC through award no. GOIPD/2022/443. This publication has emanated from research supported in part by two grants from Science Foundation Ireland under grant numbers 12/RC/2278_P2 and 20/FFP-A/8950. The Goldschmidt tolerance factor formula was corrected post initial online publication on 12.06.2023. For the purpose of Open Access, the author has applied a CC BY public copyright license to any Author Accepted Manuscript version arising from this submission.

Open access funding provided by IReL.

Conflict of Interest

The authors declare no conflict of interest.

Data Availability Statement

The data that support the findings of this study are available from the corresponding author upon reasonable request.

Keywords

electron energy loss spectroscopy, oxidation states, oxygen reduction reactions, perovskites, scanning transmission electron microscopy, structure-activity correlations

Received: December 21, 2022
Revised: February 23, 2023
Published online: March 15, 2023

[1] P. Chandran, A. Ghosh, S. Ramaprabhu, *Sci. Rep.* **2018**, *8*, 3591.
[2] Y. Li, J. Lu, *ACS Energy Lett.* **2017**, *2*, 1370.
[3] A. Ostadhossein, J. Guo, F. Simeski, M. Ihme, *Commun. Chem.* **2019**, *2*, 95.
[4] C. Song, J. Zhang, in *PEM Fuel Cell Electrocatalysts and Catalyst Layers: Fundamentals and Applications*, (Ed.: J. Zhang), Springer, London **2008**, 89.
[5] M. K. Debe, *Nature* **2012**, *486*, 43.
[6] A. Gasteiger Hubert, M. Marković Nenad, *Science* **2009**, *324*, 48.
[7] Z. W. Seh, J. Kibsgaard, C. F. Dickens, I. Chorkendorff, J. K. Nørskov, T. F. Jaramillo, *Science* **2017**, *355*, eaad4998.
[8] Y. Li, Q. Li, H. Wang, L. Zhang, D. P. Wilkinson, J. Zhang, *Electrochem. Energy Rev.* **2019**, *2*, 518.
[9] H. T. Chung, D. A. Cullen, D. Higgins, B. T. Sneed, E. F. Holby, K. L. More, P. Zelenay, *Science* **2017**, *357*, 479.
[10] Y. Liang, Y. Li, H. Wang, J. Zhou, J. Wang, T. Regier, H. Dai, *Nat. Mater.* **2011**, *10*, 780.
[11] J. Suntivich, H. A. Gasteiger, N. Yabuuchi, H. Nakanishi, J. B. Goodenough, Y. Shao-Horn, *Nat. Chem.* **2011**, *3*, 546.
[12] Y. Xue, L. Shi, X. Liu, J. Fang, X. Wang, B. P. Setzler, W. Zhu, Y. Yan, Z. Zhuang, *Nat. Commun.* **2020**, *11*, 5651.
[13] S. Liu, C. Sun, J. Chen, J. Xiao, J. L. Luo, *ACS Catal.* **2020**, *10*, 13437.
[14] N. I. Kim, Y. J. Sa, T. S. Yoo, S. R. Choi, R. A. Afzal, T. Choi, Y. S. Seo, K. S. Lee, J. Y. Hwang, W. S. Choi, S. H. Joo, J. Y. Park, *Sci. Adv.* **2018**, *4*, 9360.
[15] A. Grimaud, K. J. May, C. E. Carlton, Y.-L. Lee, M. Risch, W. T. Hong, J. Zhou, Y. Shao-Horn, *Nat. Commun.* **2013**, *4*, 2439.
[16] Z. Shao, S. M. Haile, *Nature* **2004**, *431*, 170.
[17] V. Celorrio, A. S. Leach, H. Huang, S. Hayama, A. Freeman, D. W. Inwood, D. J. Fermin, A. E. Russell, *ACS Catal.* **2021**, *11*, 6431.
[18] B. Hua, Y.-Q. Zhang, N. Yan, M. Li, Y.-F. Sun, J. Chen, J. Li, J.-L. Luo, *Adv. Funct. Mater.* **2016**, *26*, 4106.
[19] Y. Zhu, W. Zhou, J. Yu, Y. Chen, M. Liu, Z. Shao, *Chem. Mater.* **2016**, *28*, 1691.
[20] V. Celorrio, L. Calvillo, E. Dann, G. Granozzi, A. Aguadero, D. Kramer, A. E. Russell, D. J. Fermín, *Catal. Sci. Technol.* **2016**, *6*, 7231.
[21] G. S. Hegde, A. Ghosh, R. Badam, N. Matsumi, R. Sundara, *ACS Appl. Energy Mater.* **2020**, *3*, 1338.
[22] C. Zhao, X. Zhang, M. Yu, A. Wang, L. Wang, L. Xue, J. Liu, Z. Yang, W. Wang, *Adv. Mater.* **2020**, *32*, 2006145.
[23] M. Qu, X. Ding, Z. Shen, M. Cui, F. E. Oropeza, G. Gorni, V. A. de la Peña O'Shea, W. Li, D. C. Qi, K. H. L. Zhang, *Chem. Mater.* **2021**, *33*, 2062.
[24] J. Sun, L. Du, B. Sun, G. Han, Y. Ma, J. Wang, H. Huo, C. Du, G. Yin, *ACS Appl. Mater. Interfaces* **2020**, *12*, 24717.
[25] G. P. A. Gobaille-Shaw, V. Celorrio, L. Calvillo, L. J. Morris, G. Granozzi, D. J. Fermín, *ChemElectroChem* **2018**, *5*, 1922.
[26] X. Li, I. Roy, V. Chakrapani, *J. Phys. Chem. C* **2021**, *125*, 15166.
[27] W. T. Hong, M. Risch, K. A. Stoerzinger, A. Grimaud, J. Suntivich, Y. Shao-Horn, *Energy Environ. Sci.* **2015**, *8*, 1404.
[28] M. Risch, *Catalysts* **2017**, *7*, 154.
[29] J. Bak, H. Bin Bae, S. Y. Chung, *Nat. Commun.* **2019**, *10*, 2713.
[30] N. Tsvetkov, Q. Lu, L. Sun, E. J. Crumlin, B. Yildiz, *Nat. Mater.* **2016**, *15*, 1010.
[31] M. Barzilay, T. Qiu, A. M. Rappe, Y. Ivry, *Adv. Funct. Mater.* **2020**, *30*, 1902549.
[32] X. Wang, X. Li, X. Chu, R. Cao, J. Qian, Y. Cong, K. Huang, J. Wang, C. Redshaw, R. Sarangi, G. Li, S. Feng, *Adv. Funct. Mater.* **2021**, *31*, 2006439.
[33] V. Celorrio, E. Dann, L. Calvillo, D. J. Morgan, S. R. Hall, D. J. Fermin, *ChemElectroChem* **2016**, *3*, 283.
[34] K. A. Stoerzinger, M. Risch, B. Han, Y. Shao-Horn, *ACS Catal.* **2015**, *5*, 6021.
[35] V. Celorrio, L. Calvillo, G. Granozzi, A. E. Russell, D. J. Fermin, *Top. Catal.* **2018**, *61*, 154.
[36] H. Liu, C. Hu, Z. L. Wang, *Nano Lett.* **2006**, *6*, 1535.
[37] C. G. Hu, H. Liu, C. S. Lao, L. Y. Zhang, D. Davidovic, Z. L. Wang, *J. Phys. Chem. B* **2006**, *110*, 14050.
[38] K. Hayat, M. A. Rafiq, S. K. Durrani, M. M. Hasan, *Phys. B* **2011**, *406*, 309.
[39] Y. Xu, A. Tsou, Y. Fu, J. Wang, J. H. Tian, R. Yang, *Electrochim. Acta* **2015**, *174*, 551.
[40] S. Satapathy, M. K. Singh, P. Pandit, P. K. Gupta, *Appl. Phys. Lett.* **2012**, *100*, 042904.
[41] S. J. Pennycook, L. A. Boatner, *Nature* **1988**, *336*, 565.
[42] S. J. Pennycook, P. D. Nellist, in *Impact of Electron and Scanning Probe Microscopy on Materials Research*, (Eds.: D. G. Rickerby, G. Valdrè, U. Valdrè), Springer, Dordrecht **1999**, p. 161.
[43] E. Yücelen, I. Lazić, E. G. T. Bosch, *Sci. Rep.* **2018**, *8*, 2676.
[44] H. Tan, S. Turner, E. Yücelen, J. Verbeeck, G. Van Tendeloo, *Phys. Rev. Lett.* **2011**, *107*, 107602.
[45] S. Nishida, S. Kobayashi, A. Kumamoto, H. Ikeno, T. Mizoguchi, I. Tanaka, Y. Ikuhara, T. Yamamoto, *J. Appl. Phys.* **2013**, *114*, 054906.
[46] X. Cai, K. Chen, X. Gao, C. Xu, M. Sun, G. Liu, X. Guo, Y. Cai, B. Huang, J. Deng, J. Z. Liu, A. Tricoli, N. Wang, C. Dwyer, Y. Zhu, *Chem. Mater.* **2019**, *31*, 5769.
[47] R. F. Egerton, *Electron Energy-Loss Spectroscopy in the Electron Microscope*, Springer, New York **2011**.

[48] R. D. Leapman, L. A. Grunes, *Phys. Rev. Lett.* **1980**, *45*, 397.
[49] T. G. Sparrow, B. G. Williams, C. N. R. Rao, J. M. Thomas, *Chem. Phys. Lett.* **1984**, *108*, 547.
[50] M. Varela, M. P. Oxley, W. Luo, J. Tao, M. Watanabe, A. R. Lupini, S. T. Pantelides, S. J. Pennycook, *Phys. Rev. B* **2009**, *79*, 085117.
[51] L. A. J. Garvie, A. J. Craven, *Phys. Chem. Miner.* **1994**, *21*, 191.
[52] T. Riedl, T. Gemming, W. Gruner, J. Acker, K. Wetzig, *Micron* **2007**, *38*, 224.
[53] H. Tan, J. Verbeeck, A. Abakumov, G. Van Tendeloo, *Ultramicroscopy* **2012**, *116*, 24.
[54] F. Frati, M. O. J. Y. Hunault, F. M. F. de Groot, *Chem. Rev.* **2020**, *120*, 4056.
[55] S. Kobayashi, Y. Tokuda, T. Mizoguchi, N. Shibata, Y. Sato, Y. Ikuhara, T. Yamamoto, *J. Appl. Phys.* **2010**, *108*, 124903.
[56] Z. Zhang, W. Sigle, M. Rühle, *Phys. Rev. B* **2002**, *66*, 094108.
[57] N. D. Browning, H. O. Moltaji, J. P. Buban, *Phys. Rev. B* **1998**, *58*, 8289.
[58] J. H. Rask, B. A. Miner, P. R. Buseck, *Ultramicroscopy* **1987**, *21*, 321.
[59] N. Y. Kim, T. Yim, J. H. Song, J. S. Yu, Z. Lee, *J. Power Sources* **2016**, *307*, 641.
[60] R. Qiao, T. Chin, S. J. Harris, S. Yan, W. Yang, *Curr. Appl. Phys.* **2013**, *13*, 544.
[61] R. F. Klie, Y. Ito, S. Stemmer, N. D. Browning, *Ultramicroscopy* **2001**, *86*, 289.
[62] E. Marelli, J. Gazquez, E. Poghosyan, E. Müller, D. J. Gawryluk, E. Pomjakushina, D. Sheptyakov, C. Piamonteze, D. Aegerter, T. J. Schmidt, M. Medarde, E. Fabbri, *Angew. Chem., Int. Ed.* **2021**, *60*, 14609.
[63] D. Qian, B. Xu, M. Chi, Y. S. Meng, *Phys. Chem. Chem. Phys.* **2014**, *16*, 14665.
[64] M. C. Biesinger, B. P. Payne, A. P. Grosvenor, L. W. M. Lau, A. R. Gerson, R. S. C. Smart, *Appl. Surf. Sci.* **2011**, *257*, 2717.
[65] E. S. Ilton, J. E. Post, P. J. Heaney, F. T. Ling, S. N. Kerisit, *Appl. Surf. Sci.* **2016**, *366*, 475.
[66] V. Di Castro, G. Polzonetti, *J. Electron Spectrosc. Relat. Phenom.* **1989**, *48*, 117.
[67] M. Ezbiri, V. Becattini, M. Hoes, R. Michalsky, A. Steinfeld, *ChemSusChem* **2017**, *10*, 1517.
[68] K. A. Stoerzinger, M. Risch, J. Suntivich, W. M. Lü, J. Zhou, M. D. Biegalski, H. M. Christen, Ariando, T. Venkatesan , Y. Shao-Horn, *Energy Environ. Sci.* **2013**, *6*, 1582.
[69] Y. Aoki, K. Takase, H. Kiuchi, D. Kowalski, Y. Sato, H. Toriumi, S. Kitano, H. Habazaki, *J. Am. Chem. Soc.* **2021**, *143*, 6505.
[70] Y. Q. Lyu, F. Ciucci, *ACS Appl. Mater. Interfaces* **2017**, *9*, 35829.
[71] X. Long, P. Yu, N. Zhang, C. Li, X. Feng, G. Ren, S. Zheng, J. Fu, F. Cheng, X. Liu, *Nanomaterials* **2019**, *9*, 577.